J Mater Sci: Mater Electron

Coexistence of the electric polarization and conductive current in the bismuth–neodymium ferrite garnet films

S. S. Aplesnin[1], A. N. Masyugin[1,*], M. N. Volochaev[1,2], and T. Ishibashi[3]

[1] Reshetnev Siberian State University of Science and Technology, Krasnoyarsk, Russia
[2] Kirensky Institute of Physics, Federal Research Center KSC SB RAS, Krasnoyarsk, Russia
[3] Department of Materials Science and Technology, Nagaoka University of Technology, Nagaoka, Niigata 940-2188, Japan

Received: 31 October 2020
Accepted: 14 December 2020

© The Author(s), under exclusive licence to Springer Science +Business Media, LLC part of Springer Nature 2021

ABSTRACT

The $Nd_1Bi_2Fe_5O_{12}/Nd_2Bi_1Fe_4Ga_1O_{12}$ polycrystalline films on the glass substrate and the $Nd_{0.5}Bi_{2.5}Fe_5O_{12}$ epitaxial films on the single-crystal gadolinium gallium garnet substrate have been investigated by impedance and dielectric spectroscopy. The inductive contribution to the impedance and two relaxation channels related to ferroelectric domains and migration polarization have been established. The magnetocapacitance and magnetoimpedance have been determined. The conductive and polarization currents and the phase difference between them for the films of two types have been determined. The critical temperatures of the polarization disappearance and hysteresis I–V have been found. A model of the polarization caused by the piezoelectric effect and flexoelectric interaction has been proposed. I–V hysteresis is explained by the presence of ferroelectric domains near the interface and is associated with the hysteresis of the electric polarization.

1 Introduction

Study of materials for spintronic [1, 2] and memristor [3, 4] devices are interesting for both fundamental research and application. In recent years, along with conventional storage devices, much attention has been paid to the resistive memory, which combines the advantages of fast random-access memory and nonvolatility of programmable memory. The resistance of a memristor depends on the charge passed through it. Most memristors are based on metal–insulator–metal tunnel structures with the oxygen nonstoichiometry [5, 6]. The ion drift under the applied voltage changes the electrical resistance.

Another fundamental problem is how the current can be controlled by electrical polarization. Ferroelectrics are dielectrics. The conductivity and ferroelectricity are two mutually exclusive factors. This problem can be solved by creating electrically inhomogeneous states. In part of the volume of the material, electric polarization is realized, the other part is a semiconductor. The coexistence of ferroelectric and semiconductor properties can be observed in multiferroics with the magnetoelectric coupling. The magnetoelectric coupling was

Address correspondence to E-mail: albert.masyugin@mail.ru

https://doi.org/10.1007/s10854-020-05121-9
Published online: 09 January 2021

observed in the bismuth ferrite garnet films [7]. The Curie temperature has been estimated to be around 650 K [8].

In the 10-μm-thick $(BiLu)_3(FeGa)_5O_{12}$ films grown by the liquid-phase epitaxy on a $Gd_3Ga_5O_{12}$ substrate with the (210) orientation, the motion of magnetic domain walls under the action of an electric field [9] and switching of their electric polarization in a magnetic field [10] were found, which are not observed in films with the (111) substrate orientation. These effects are explained by the inhomogeneous magnetoelectric interaction and the magnetic anisotropy variation in an electric field [11–13]. The anomalously strong linear magnetoelectric effect was observed in the ferrite garnet epitaxial films in magnetic fields of up to 5 kOe in [14] and attributed by the authors to the nonuniform film straining caused by the substrate. The linear magnetoelectric (ME) effect with a maximum at 450 K found in the 90-nm-thick $Bi_3Fe_5O_{12}$ films by electric field-modulated ferromagnetic resonance was explained by the strong spin–orbit coupling and the formation of local magnetic inhomogeneity and directly attributed to bismuth ions [15]. The linear ME effect is determined from the magnetization variation in an electric field. The electric polarization of the magnetic field-induced bismuth iron garnet (BIG) films is caused by the bilinear EH and quadratic EH^2 effect [16].

The electric polarization can be caused by structural deformation leading to the violation of the inversion center under epitaxial stresses in a film on the substrate or cationic substitution over dodecahedral sites, surface electronic states, and a magnetic domain structure caused by demagnetizing fields and the spin–orbit interaction. The electric polarization results from the piezoelectric effect, which can be induced by an electric field in a nonpolar (centrosymmetric) dielectric. An electric field, due to electrostriction, transforms the structure of any isotropic dielectric into noncentrosymmetric one, inducing the electromechanical coupling (piezoelectric activity) in it. The piezoelectric effect in dielectrics can be induced by an electric field.

The strain gradient can also lead to the polarization due to the flexoelectric effect. According to the microscopic theory of the flexoelectric effect, in the case of a static deformation gradient, it was found to be weaker by four orders of magnitude than the experimental value for the coupling between the polarization amplitudes and the deformation gradient in an acoustic wave in diamond-type structures [17]. Since the elastic stresses are almost always induced in films, this effect must be taken into account in the presence of weak polarization. The effect of epitaxial stresses can be elucidated using two types of substrates and different substitutes (neodymium and gallium).

The calculation of the BIG electronic structure using the electron density functional theory with allowance for the relativistic corrections showed the enhancement of the spin–orbit coupling due to the hybridization of 6p bismuth orbitals with oxygen and iron ions [18]. The experimental splitting value t_{2g} of the states of iron ions under the spin–orbit interaction is 39.4 mV [19]. The nuclear magnetic resonance (NMR) study of the $Bi_3Fe_5O_{12}$ compound showed a magnetic moment of $0.1\mu_B$ per bismuth atom due to the hyperfine interaction and sp hybridization of the Bi–O orbitals [20]. The electron density shift on the Bi–O bond will induce the dipole moment and electric polarization.

The linear response of the ME susceptibility is caused by the spin–orbit interaction and the ME effect quadratic in the magnetic field is driven by the exchange striction. The bismuth–neodymium ferrite garnet films are characterized by a maximum in the magnetostriction, which changes its sign upon temperature variation [21]. Carriers in the single-crystal film are induced by the film growth defects; in the polycrystalline film, defects can occur at the grain boundaries in the anionic subsystem.

The aim of this study is to establish the mechanism of electric polarization and the possibility of existence of a conductive current in bismuth-substituted ferrite garnet films, since the conductivity and ferroelectricity are two mutually exclusive factors.

2 Electron and optical spectroscopy investigations

The object of study was the $Nd_1Bi_2Fe_5O_{12}/Nd_2Bi_1Fe_4Ga_1O_{12}$ polycrystalline films on a glass substrate and the $Nd_{0.5}Bi_{2.5}Fe_5O_{12}$ epitaxial films grown on a single-crystal gadolinium gallium garnet (GGG) substrate in the (111) crystallographic direction. The films were obtained by decomposition of the metalorganic compound from melt [22]. The method of metal organic decomposition (MOD) consists in spin coating a solution of organometallic compounds,

mixed in accordance with the required stoichiometry of the film composition and followed by annealing. MOD, unlike dc sputter deposition, does not require expensive vacuum equipment. It is difficult to obtain films with the necessary stoichiometric composition and high substitution of bismuth by the method of sputtering on direct current [23], due to the high volatility of Bi. Homogeneous highly Bi-substituted iron garnet films can be prepare using only MOD method. Impurity phases were found in polycrystalline BIG films prepared by reactive ion beam sputtering method [24].

The magnetic hysteresis loops were recorded in fields of up to 2 kOe applied perpendicular and parallel to the film surface. The magnetic moment saturation field was 0.75 kOe and the saturation magnetization in the film plane was stronger than the magnetization along the film normal by 15% [26]. A bilayer film is deposited onto the glass substrate. Using the bilayer film enable to switch the direction of the magnetic moment and modulate the value of the Faraday angle of rotation in a magnetic field [27]. The Faraday effect depends on the magnetization of the films, which is determined by the magnetic anisotropy. The film $NdBi_2Fe_4GaO_{12}$ on glass have perpendicular magnetic anisotropy and showed large Faraday rotation angles. The $Nd_1Bi_2Fe_5O_{12}$ film has in-plane magnetic anisotropy and a smaller Faraday rotation angle.

Specimens for the transmission electron microscopy (TEM) investigations on a Hitachi FB-2100 focused ion beam system were prepared in the cross-sectional geometry. The TEM study was carried out on a Hitachi HT 7700 microscope at an accelerating voltage of 110 kV. The TEM data are presented in Fig. 1. The film on the GGG substrate has a thickness of about 380±10 nm and grows epitaxially, which was confirmed by the microdiffraction pattern, but contains microcavities from several to tens nanometers in size. The presence of bubble inclusions in the structure of the films may be due to gassing of CH_3 found by IR spectra in the process of decomposition of organometallic decomposition during annealing [25]. The filtered high-resolution image shows a sharp interface between the film and the substrate. Diffuse spots in the diffraction pattern are indicative of the mismatch between the lattice parameters of the film and GGG substrate.

Defect states are determined from IR spectra. The IR absorption spectrum of the polycrystalline film on glass was measured by an FSM2202 IR Fourier spectrometer in the frequency range of 2000–7500 cm^{-1}; below 2000 cm^{-1}, glass strongly absorbs the far-IR radiation (Fig. 2). The absorption line at a frequency of 3570 cm^{-1} is asymmetric and related to the vibrations of the OH groups. In water, the O–H bond vibrations have three peaks at frequencies of 3080, 3440, and 3670 cm^{-1} at the qualitatively preserved symmetry relative to the central peak [28]. The frequency of the vibrations of hydroxyl groups in the water molecule increases upon heating under standard conditions [29]. In the films, the absorption frequency is temperature-independent up to 500 K. The difference of the spectra from water is caused by the fact that, in the vapor phase, the average size of a cluster containing H_2O molecules is 630 molecules [30]. The distance between oxygen atoms is 0.45 nm [31]; then, a film microcavity contains one cluster and the liquid–vapor transition does not occur up to 500 K. The weak absorption maximum at a frequency of 6020 cm^{-1} (1.66 μm) is related to bivalent iron ions split by a low-symmetry crystal field. The triplet $^5T_{2g}$ state of Fe^{2+} ions in a tetrahedron with triclinic lattice distortion is split into a $^5E_{g1}$ doublet and an A_g singlet. In the model of the crystal field with parameters 10Dq=9500 cm^{-1}, trigonal splitting C=500 cm^{-1}, the electronic transition to A_g—^5E_g at a wavelength of 1.66 μm in the tetrahedron in the ferrite of the grant is calculated [32]. Thus, the conductivity is due to the divalent iron ions. The absorption peak at a frequency of 2750 cm^{-1} corresponds to the symmetric stretching vibrating of C=H atoms in methane.

The absorption spectrum in the optical range was measured on a Cary500Scan spectrophotometer (Fig. 3). The bandgap Eg was determined as a difference between the electron and hole localization thresholds [33].

$$\alpha = \frac{A(h\nu - E_g)^{\frac{1}{2}}}{h\nu} \quad (1)$$

where A is the parameter, hν is the photon energy, E_g is the optical bandgap energy, and α is the absorption coefficient. The energy bandgaps of the films estimated from the tangent lines in the plot of $(\alpha h\nu)^2$ versus photon energy $h\nu$ for direct-gap semiconductors (Fig. 3a) are E_g=2.34 eV for the films on GGG and E_g=2.27 eV for the films on glass. In the films on the GGG substrate with the high (16%) neodymium content, the maximum in the conduction band is observed.

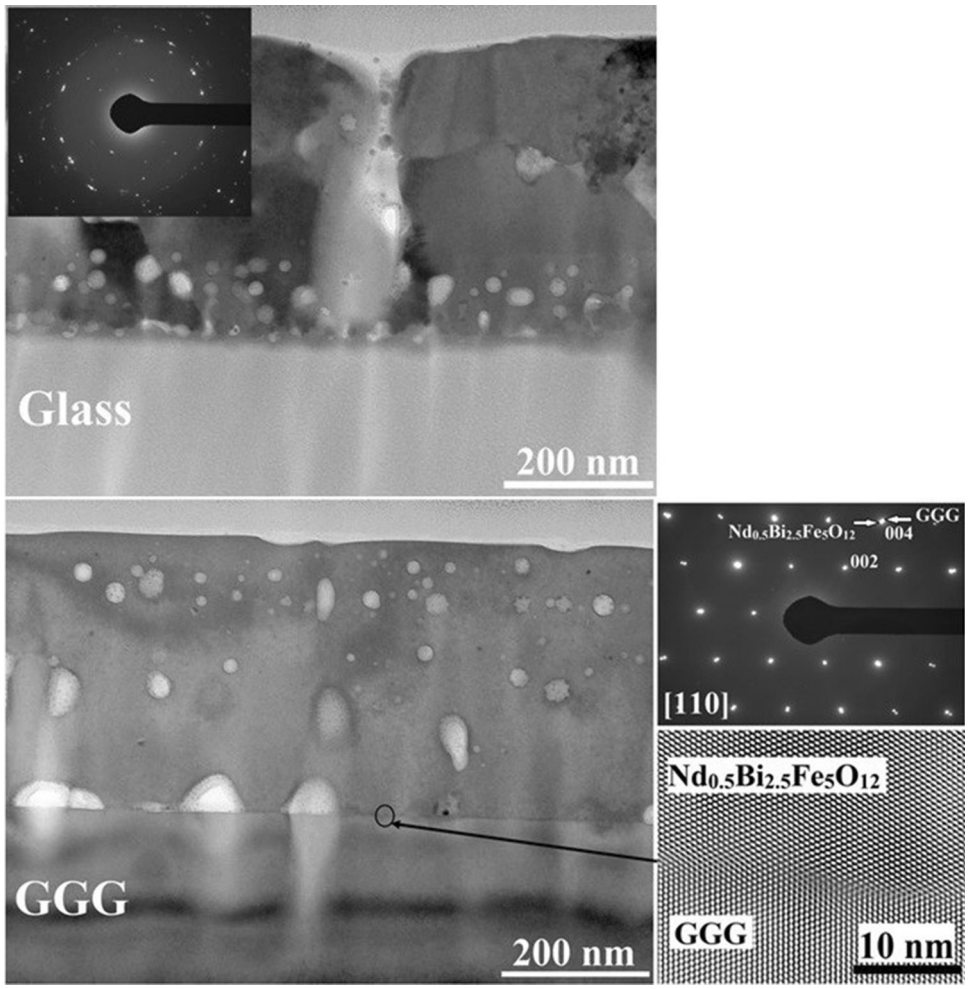

Fig. 1 Morphology and X-ray of a film on a garnet (down) on glass (up) using a transmission electron microscope

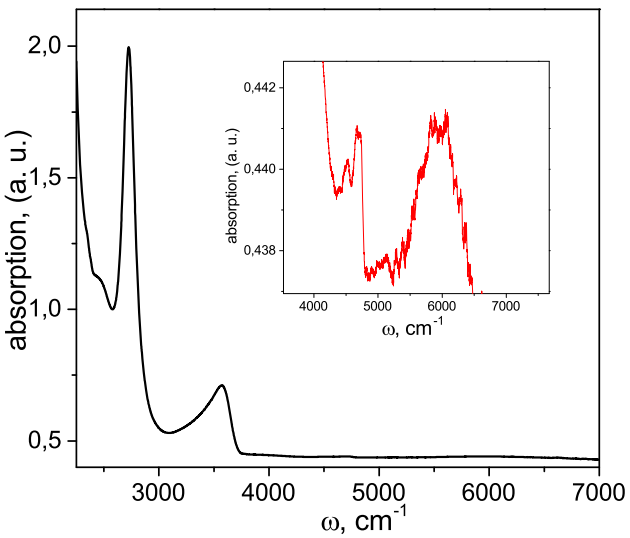

Fig. 2 IR absorption of a polycrystalline film on glass. Inset: IR absorption in the frequency range 4000–7000 cm^{-1}

This maximum consists of two peaks with energies of 2.66 and 2.81 eV, which are caused by the electronic transitions $^4I_{4/2}$–$^4G_{9/2}$ and $^4I_{4/2}$–$^4G_{11/2}$ on Nd^{3+} ions [34]. With increasing concentration of neodymium ions, the splitting of terms vanishes due to the hybridization of the electronic states with iron ions and formation of the band states. Substitution of neodymium for bismuth slightly narrows the bandgap as compared with a value of E_g=2.85 eV for the $Bi_3Fe_5O_{12}$ film [35].

According to the results of the fully relativistic ab initio calculation using the density functional theory [18, 36], the bismuth subbands with 6P J=1/2 and J=3/2 split into dE=1.3 eV. The lower subband width is 1 eV and the absorption minimum should be observed above 4 eV. In the bandgap of the film, there are small absorption maxima at frequencies of ω_1=9300 cm^{-1} (E_1=1.15 eV) and ω_2=14,100 cm^{-1} (E_2=1.74 eV). The electronic transitions between the Nd^{3+} multiplets in GGG do not occur in this frequency

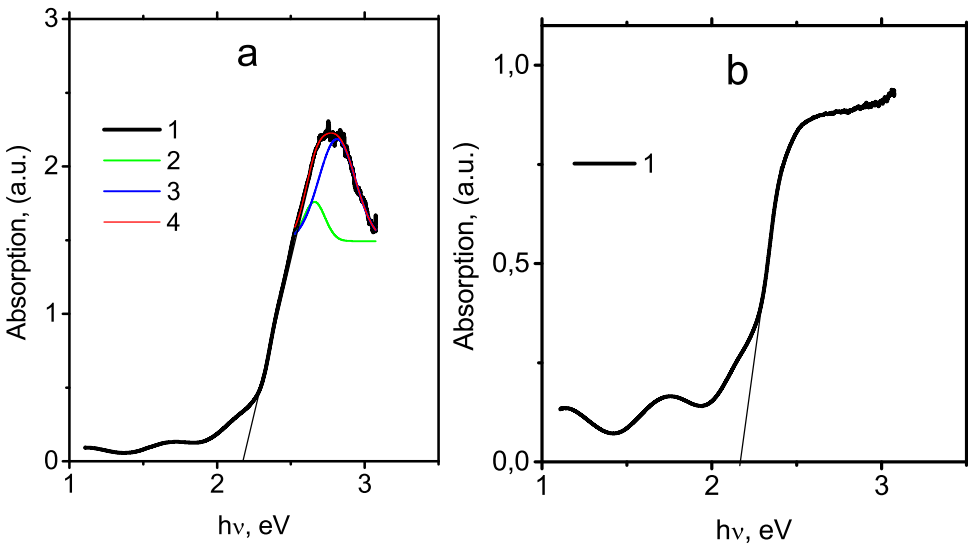

Fig. 3 Optical absorption spectrum of $Nd_{0.5}Bi_{2.5}Fe_5O_{12}$ films on a GGG single-crystal substrate (1), Gaussian function: peak 1 (2), peak 2 (3) and sum (4) (**a**) and $Nd_1Bi_2Fe_5O_{12}$/ $Nd_2Bi_1Fe_4Ga_1O_{12}$ on a glass substrate (**b**)

range [34] and the low-frequency transitions ${}^6A_1 \rightarrow {}^4T_2$, ${}^4E$, and ${}^4T_1$ in YGG: Fe (6.2 at %) on iron ions in the octahedral positions with E_1=1.3 eV and E_2=1.77 eV are observed [37]. The occurrence of these transitions points out that the investigated compounds belong to Mott semiconductors with a charge gap formed by oxygen ions. The charge is transferred through the Fe–O–Fe bond. The presence of oxygen vacancies will lead to the growth of the conductivity.

3 Impedance and capacitance

Impedance spectroscopy provides information on the interface and electric charges with different degrees of localization. Figure 4 shows the active (R= ReZ) and reactive (X=*Im Z*) parts of the impedance of the film on the GGG substrate as functions of temperature measured in the configuration with two contacts on the film surface (the ac current along the film). The $X(T)$ behavior in the range of 10^3–10^6 Hz is frequency-independent and the normalized values of the reactive part of the impedance $X(T)/X$ (T=80 K) hit one curve. In the temperature range of 180–215 K, the reactance decreases by 5% and the active resistance at frequencies of ω>100 kHz doubles. In this temperature range, the thermal expansion coefficient has a maximum. The mismatch between the substrate and film lattice parameters induces elastic stresses and shear strains at the interface, which leads to a change in the magnetic anisotropy. The energy of magnetic anisotropy in most garnet ferrites consists of two parts that are comparable in magnitude: the magnetic anisotropy of the undeformed crystal lattice and the anisotropy caused by the magnetoelastic interaction, which differ in sign. This leads to an anomalous temperature dependence of the anisotropy constant, namely, to a change in sign. A change in the sign of the magnetostrictive deformation at 300 K in films [38] will lead to a spin–reorientation transition. In rare-earth ferrite garnets $Re_3Fe_5O_{12}$ (R= Tb, Er, Sm), spontaneous orientational transitions are observed at T ~ 200 K, 66 K [39].

The experimental data can be qualitatively described using the Debye model:

$$\begin{aligned} \mathrm{Re}Z(\omega) &= \frac{A}{1+(\omega\tau_1)^2} + \frac{B}{1+(\omega\tau_2)^2}, \\ \mathrm{Im}\ Z(\omega) &= \frac{A\omega\tau_1}{1+(\omega\tau_1)^2} + \frac{B\omega\tau_2}{1+(\omega\tau_2)^2} \end{aligned} \quad (2)$$

where A and B are the constant parameters and $\tau_{1,2}$ are the relaxation times the temperature dependence of which is described by the exponent $\tau_{1,2}=\tau_{1,2,0}$ exp ($\Delta E_{1,2}/T$) with activation energies of ΔE_1=69 mV (560 cm^{-1}) and ΔE_2=180 mV (1450 cm^{-1}). The lowest activation energy corresponds to the vibrations of the tetrahedral group in the yttrium iron garnet at a frequency of 620 cm^{-1}. Substitution of heavy element bismuth for yttrium reduces the vibration frequency in the lattice. The quantity ΔE_2 characterizes the energy of the elastic stress gradient in the film.

The temperatures of the broad $R(T)$ maxima and the $X(T)$ inflection points in the range of 260–275 K are weakly frequency-dependent. This can be related to an orientational transition of the magnetization in the bulk of the film. The magnetostriction constant

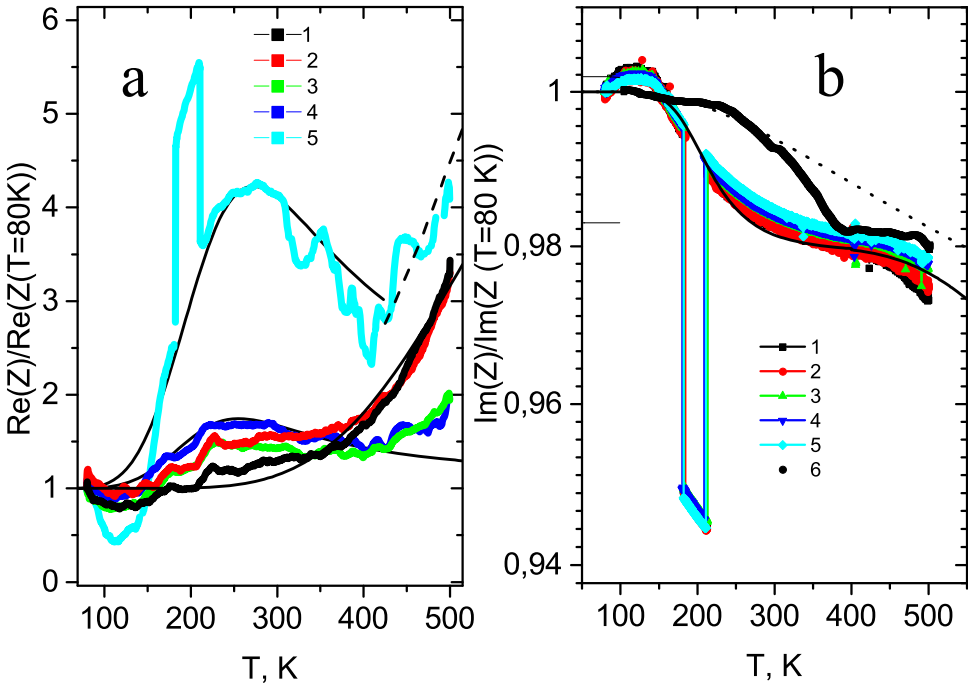

Fig. 4 Normalized value of active *Re* (*Z*)/*Re* (*Z* (*T*=80 K)) (**a**) and reactive *Im* (*Z*)/*Im* (*Z* (*T*=80 K)) (**b**) resistance of a single-crystal film on GGG versus temperature at frequencies ω=5 kHz (1), 10 kHz (2), 50 kHz (3), 100 kHz (4), 300 kHz (5). The normalized value of capacitance *C* (*T*=80 K)/ *C* (*T*) (6) versus temperature at a frequency ω=5 kHz (**b**). Fitting functions in the Debye model (2) (lines)

changes its sign from negative to positive [21] and the quadratic ME effect dominates in the magnetoelectric interaction [16]. The temperature behaviors of the capacitance $C(T=80\ \text{K})/C(T)$ and reactance (Fig. 4b) are qualitatively different. The relaxation time $\tau_1=\tau_0 \exp(\Delta E_1/T)$ determined from the capacitance has the lower activation energy: $\Delta E_1=35$ mV. This difference is caused by the change in the inductance, since the reactive part of the impedance is caused by the capacitance and inductance. The inductive contribution occurs from the change in the magnetic induction $dB/dt=dM/dt$ related to the polarization $M=aP+bP^2$ via the magnetoelectric interaction. The induction voltage $\varepsilon_i=-d\Phi/dt=c+dP$ is determined by the tensor of the linear and quadratic ME interaction. The inductance jump in the range of 180–215 K is caused by the magnetic order rearrangement at the film–substrate interface. The change in the elastic stresses at the interface upon heating results in the change in the anisotropy field. The orientational transition at the surface leads to an increase in the amplitude of the magnetic moment oscillations.

The impedance components for the polycrystalline film on the glass substrate are temperature-independent up to 225 K and have a jump at 302 K with a slight anomaly at 370 K (Fig. 5). Above 150 K, the inductive contribution is added to the reactive part of the impedance, so the difference $[X(T)/X(T=80)]-[C(T=80)/C()]$ is 0.6%, which is twice as small as the value for the film on GGG. The ME interaction tensor changes its sign in the polycrystalline film above room temperature [16], which leads to the change in the inductance sign. Above 300 K, the temperature dependence of the impedance components is described using Debye model (2) with the same activation energy as in the case of the film on GGG. Therefore, the impedance anomaly and relaxation time are independent of the substrate type and are driven by the same mechanism. The impedance jump is caused by the inductive contribution resulting from the spin–reorientation transition.

Since the reactive part of the impedance is higher than the ac resistance by two orders of magnitude, the frequency dependence of the impedance qualitatively coincides with *Im*(*Z*). At *T*=300 K, in the frequency range of 10^2–10^6 Hz, at $\omega\tau>>1$, Eq. (1) is reduced to $Im(Z)=A/\omega\tau$. In the model of equivalent circuits, the impedance hodograph of the film on glass is described by one *RC* contour (Fig. 6). Using the impedance hodograph, we find the relaxation times $\tau=RC$ to be $\tau=0.08$ s at *T*=340 K and $\tau=0.003$ s at 380 K (Fig. 6b). These values are typical of the migration polarization.

The effect of the magnetic field on the impedance components is observed in the high-frequency region $\omega>100$ kHz, which exceeds a frequency of migration polarization of 10^5 Hz. Figure 7 shows the impedance components Im(*Z*) and Re(*Z*) as functions of the

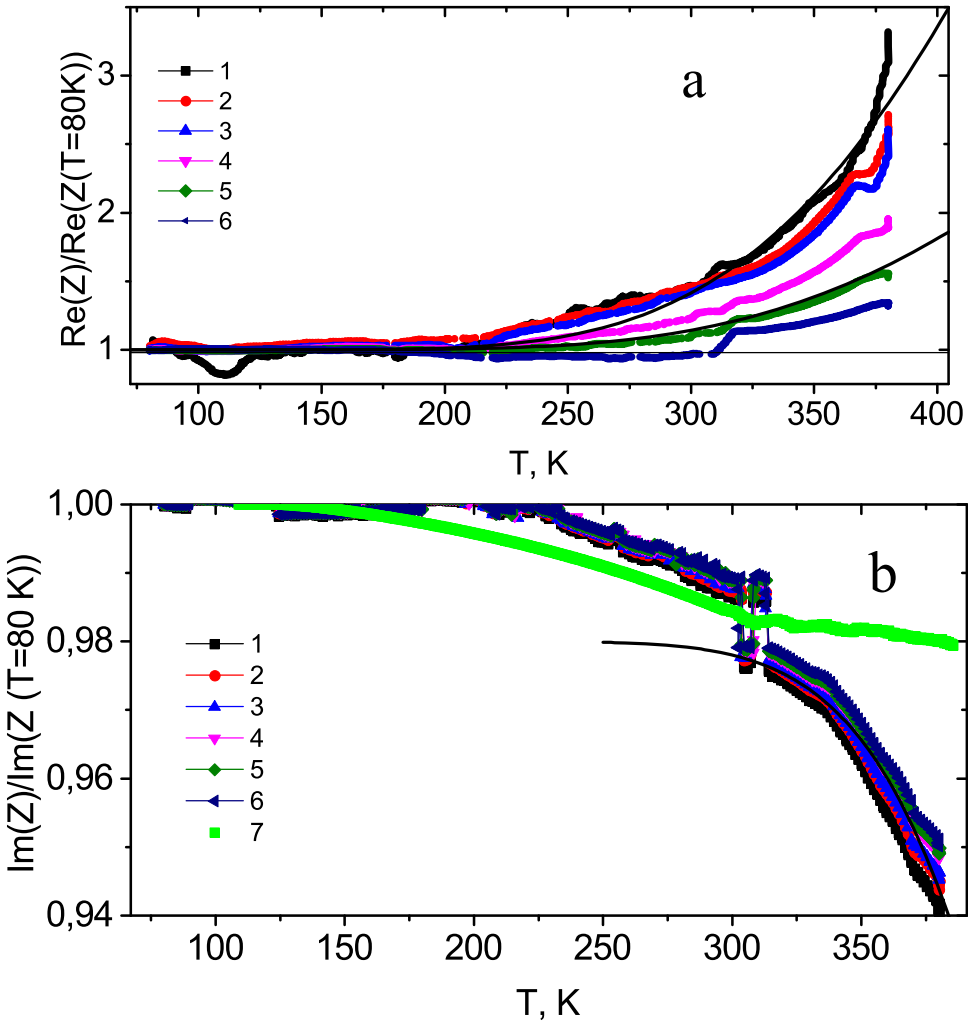

Fig. 5 Normalized value of active *Re* (*Z*)/*Re* (*Z* (*T*=80 K)) (**a**) and reactive *Im* (*Z*)/*Im* (*Z* (*T*=80 K)) (**b**) resistance of the polycrystalline film on glass versus temperature at frequencies ω=1 kHz (1), 5 kHz (2), 10 kHz (3), 50 kHz (4), 100 kHz (5), 300 kHz (6). The normalized value of capacitance *C* (*T*=80 K)/*C* (T) (7) versus temperature at a frequency ω=5 kHz (**b**). Fitting functions in the Debye model (2) (solid line)

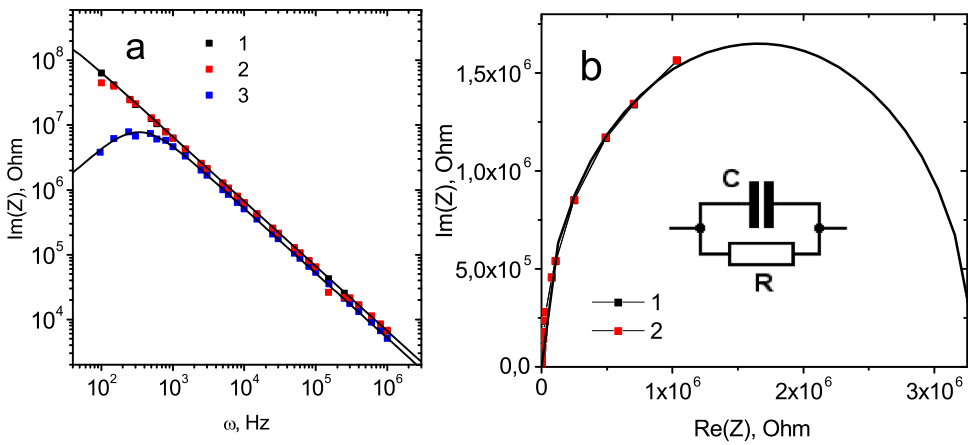

Fig. 6 Reactive part of the film impedance on glass versus frequency at *T*=300 K (1), 340 K (2), 380 K (3) (**a**). The hodograph of the film impedance on glass without a magnetic field (1) and in the field (2) at *T*=340 K. Equivalent circuit RC circuit (line) (**b**)

magnetic field at a frequency of 300 kHz. A decrease in the real part of the impedance in a magnetic field is well described by the function

$$\frac{Re(Z(H))}{Re(Z(H=0))} = 1 - \frac{AH^2}{1+H^2} \tag{3}$$

and the functional $Z(H)$ dependence correlates with the magnetization curve of the BIG films [26]. This

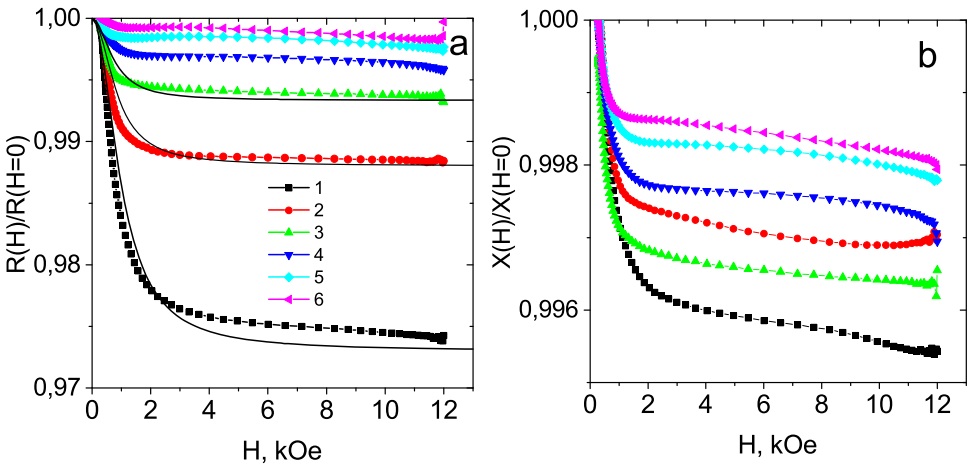

Fig. 7 Normalized values of active $R\,(H)/R\,(H=0)$ (**a**) and reactive $X\,(H)/X\,(H=0)$ (**b**) parts of the impedance at temperatures $T=160$ K (1), 200 K (2), 240 K (3), 300 K (4), 340 K (5), 380 K (6) versus the magnetic field at a frequency of 300 kHz. The fitting function on the basis of expression (3) (solid line)

effect can be explained using the model of ferroelectric domain wall with a resonance oscillation frequency of 1–10 MHz. Upon approaching the resonance frequency, the absorption of electromagnetic radiation increases. The ferroelectric walls interact with magnetic domain walls and a part of the energy of vibrations of the ferroelectric walls passes into the magnetic system. With an increase in the magnetic field, the density of magnetic domain walls decreases, which weakens the absorption of electromagnetic radiation. The reactive part of the impedance has the form $\mathrm{Im}(Z)=X_L-X_C$, where the inductive resistance X_L is determined by the magnetic domains and domain walls. Therefore, in a magnetic field, the reactive part of the impedance decreases (Fig. 7b).

Figure 8 shows the magnetocapacitance $\Delta C/C=(C(H)-C(0))/C(0)$ for the films on GGG and glass. The $\Delta C/C$ value has anomalies at 200 and 350 K for the film on GGG and at 300 K for the film on glass. The magnetocapacitance vanishes in the range of 450–470 K. The capacitance growth in a magnetic field is related also to the ME effect $P=\alpha E+bM^2$, where b, in the general case, is a tensor and determined by the variation in the exchange under the elastic stresses (the exchange striction mechanism). The value of tensor b depends on temperature [16]. Below, we show that the electric polarization vanishes above 460 K, which leads to the disappearance of the magnetocapacitance.

In the temperature range of 370–390 K, the capacitance of the film on the GGG substrate has a kink and the dielectric loss is maximum (Fig. 9). The absorbed electromagnetic radiation power decreases with increasing frequency. At these temperatures, the

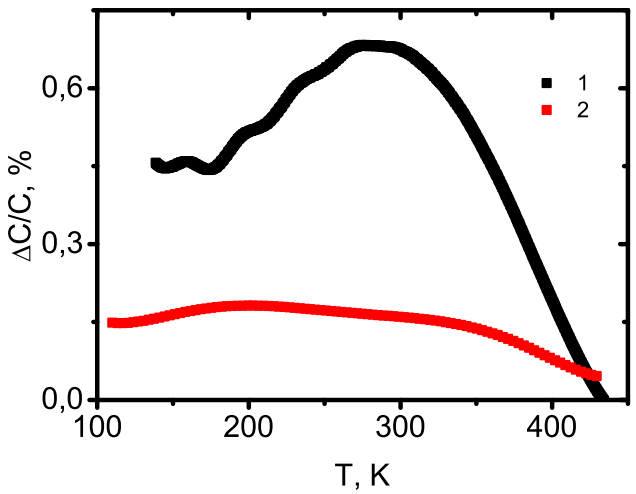

Fig. 8 Magnetocapacitance $\Delta C/C$ of the film on glass (1) and on garnet (2) versus temperature at a frequency $\omega=100$ kHz

dc resistance decreases stepwise by 10%. The capacitance and the dissipation factor are described using the Debye model as

$$\mathrm{Re}\varepsilon(\omega)=\frac{A}{1+(\omega\tau_1)^2},\ \mathrm{Im}\varepsilon(\omega)=\frac{A\omega\tau_1}{1+(\omega\tau_1)^2}, \qquad (4)$$

where τ_1 is the relaxation time, the temperature dependence of which is described by the Arrhenius law $\tau_1=\tau_0\ \exp(\Delta E_1/\mathrm{kT})$ (Fig. 9) with an activation energy of $\Delta E_1=70$ mV and a relaxation time of $\tau_1=10^{-3}$ s at $T=390$ K.

The polycrystalline film on glass exhibits several C (T) anomalies at $T=300$, 375, and 420 K without dielectric loss maxima at 300 and 420 K (Fig. 10). The small maxima and C(T) jumps are related to the change in the thermal expansion coefficient of the film relative to the glass [21]. In particular, at 420 K, the expansion of the film changes for its compression.

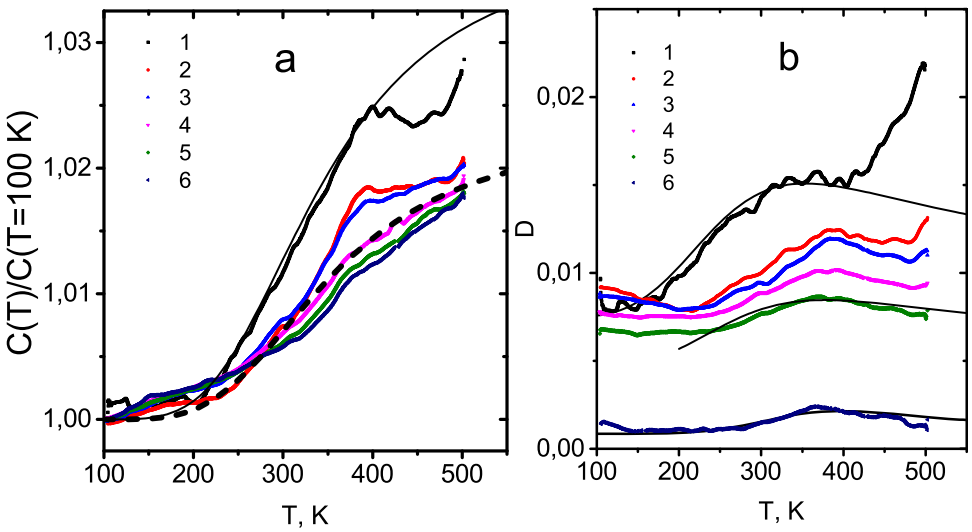

Fig. 9 Normalized value of capacitance per capacitance at T=100 K (**a**) and the dielectric loss tangent (**b**) of a film on a garnet at frequencies ω=1 kHz (1), 5 kHz (2), 10 kHz (3), 50 kHz (4), 100 kHz (5), 300 kHz (6) versus temperature. Fitting function in the Debye model (4) (solid line)

The temperature of the anomalies in the dielectric characteristics at 375 K is independent of the substrate type and correlates with the temperature of a sharp change in the electrical resistance of the films by 17% and 10% (Fig. 13). The anomalies in the electrical and dielectric properties observed at this temperature are characteristic of the film itself and independent of the substrate type. Perhaps these anomalies are associated with the Jahn–Teller transition in Fe^{2+} ions in tetrahedra and electron delocalization upon heating. The high temperature $C(T)$ and $D(T)$ maxima at $T \sim 475$ K are almost frequency-independent in the range of 1–50 kHz and disappear at higher frequencies (Fig. 10). In the case of the single-crystal film, there is no anomaly in this temperature range. This effect is related to the migration polarization over anion vacancies found in the IR spectra.

The electric polarization induced by the piezoelectric effect and the migration polarization have different frequencies. We establish the polarization types from the frequency dependence of the permittivity. Figures 11 and 12 shows the frequency dependences of the capacitance and the dissipation factor. Up to room temperatures, the $C(\omega)$ dispersion is not observed up to $\omega=10^5$ Hz for both films. In the high-frequency range, the permittivity of the films on both GGG and glass is well described by Debye model (1) with a relaxation time of $\tau=(1–3)\cdot10^{-7}$ s and, in the low-frequency range, by the relaxation time spectrum with $\tau_1=3\cdot10^{-4}$ s, $\tau_2=4\cdot10^{-5}$ s, and $\tau_3=2\cdot10^{-7}$ around room temperatures. At T>400 K, the dielectric loss in the low-frequency region is several times higher than the loss in the high-frequency region (inset in Fig. 11) and decreases in a magnetic field. In the megahertz range, the capacitance and dielectric loss decrease by a factor of 2 upon heating above 400 K. The capacitance and loss are induced by domains with the dipole polarization and, at T> 300 K, the contribution of migration polarization is added. The migration polarization dominates above 400 K.

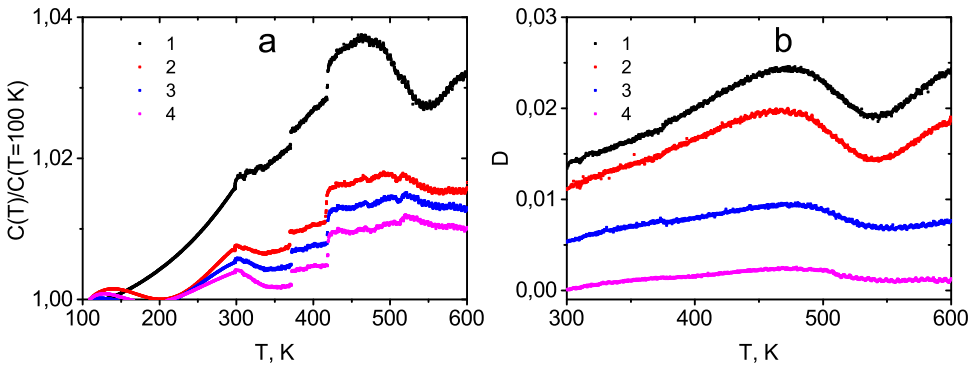

Fig. 10 Normalized value of the capacitance per capacitance at T=100 K (**a**) and the dielectric loss tangent (**b**) of the film on glass at frequencies ω=5 kHz (1), 50 kHz (2), 100 kHz (3), 300 kHz (4) versus temperature

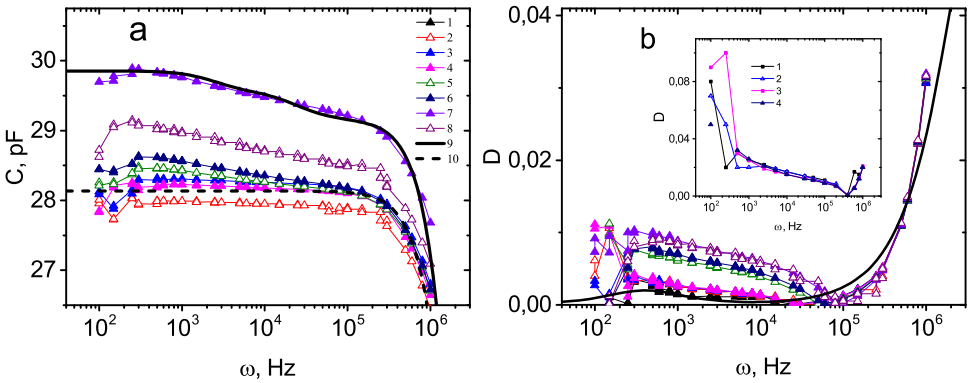

Fig. 11 Film capacitance on the glass (**a**) and the dielectric loss tangent (**b**) versus frequency at T=300 K at T=80 K: cooled at E=2000 V/cm (1), H=0 kOe cooled at H=0 kOe (2), H=12 kOe cooled at H=12 kOe (3), H=0 kOe cooled at H=12 kOe (4); at T=300 K: H=0 kOe heated at H=0 kOe (5), H=12 kOe heated H=0 kOe (6); at T=320 K: before cooling at E=2000 V/cm (7), after cooling-heating at 2000 V/cm (8); The dielectric constant in the Debye model with one relaxation time (10) and three relaxation times (9)

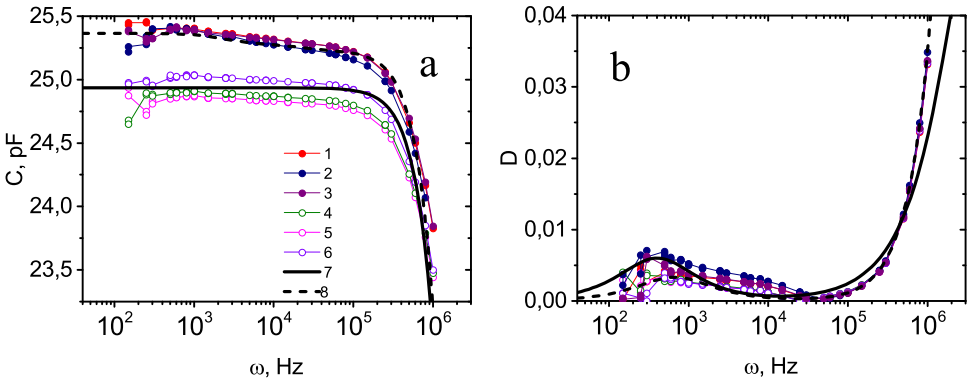

Fig. 12 Film capacitance on the garnet (**a**) and the dielectric loss tangent (**b**) versus frequency at T=300 K, H=12 kOe (1), T=320 K (2), after cooling-heating at E=2000 V/cm (3), T=80 K, after cooling at H=12 kOe, H=0 (5), H=12 kOe (4) after cooling at E=2000 V/cm, H=12 kOe (6). The dielectric constant in the Debye model with one relaxation time (7) and three relaxation times (8)

In the polycrystalline film on glass, defects and vacancies near which the impurity electrons are localized are distributed mainly inside grain boundaries. Annealing of the film in an external electric field can reduce the electric charge inside the boundaries. Upon cooling in an electric field applied perpendicular to the film, the capacitance changes. The cooling–heating cycle performed in an external electric field of 2000 V/cm reduces the capacitance by 2.6%. Cooling to 80 K in a field of 2000 V/cm enhances the capacitance by 0.5% and, in a field of 12 kOe, by 0.9% (Fig. 11). The capacitance growth is caused by the change in the polarization of ferroelectric domains under the action of magneto- and electrostriction. The magnetic capacitance at T=80 K upon cooling in magnetic and electric fields decreases by 30% and 20%, respectively (Fig. 11b). These facts are indicative of a significant effect of the prehistory of the polycrystalline film on its dielectric characteristics, which can be controlled by external fields.

In the single-crystal film grown on GGG (Fig. 12), the opposite trend is observed: upon cooling to 80 K in an electric field, the 0.5% capacitance growth exceeds the value observed upon cooling in a magnetic field. The heating–cooling cycle returns to the initial state with a change in the capacitance by smaller than 0.1%. The effect of the prehistory of the single-crystal film on the capacitance is weaker by an order of magnitude than in the polycrystalline film on glass. The magnetocapacitance $(C(H)–C(0))/C(0)$ determined at a constant temperature grows upon cooling in a magnetic field.

4 *I–V* characteristics and resistance

The dc electric properties of the films were examined by the two-probe method using an Agilent Technologies 34410A multimeter at temperatures of 80–500 K. The temperature dependences of the electrical resistance of the films on glass and GGG become drastically different below 400 K (Fig. 13): the dependence R(T) for the film on GGG increases stepwise, while the dependence for the film on glass passes through a maximum. In a single-crystal film on GGG, one can restrict oneself to two types of Fe^{2+} defects in octahedral and tetrahedral sites, which form impurity states in the bandgap with two activation energies. At the heating, the chemical potential pass through one of the levels, which leads to an increase in the activation energy. In these films can be determined the charge transport current and the polarization current from the *I–V* hysteresis.

Figure 14 shows the *I–V* characteristics of the films on GGG. We can see the *I–V* hysteresis shifted along the voltage and current axes to 280 K; i.e., there is a constant electric field, as in electrets, which induces a weak current. The bias field determined as the hysteresis asymmetry relative to the origin of coordinates passes through a maximum upon heating and sharply decreases at 280 K (Fig. 15). Decreasing the bias field in a magnetic field by a factor of 2 at low temperatures is consistent in temperature with the crystalline symmetry lowering in yttrium iron garnet at T =130 K [40] and with the maximum ME effect in the

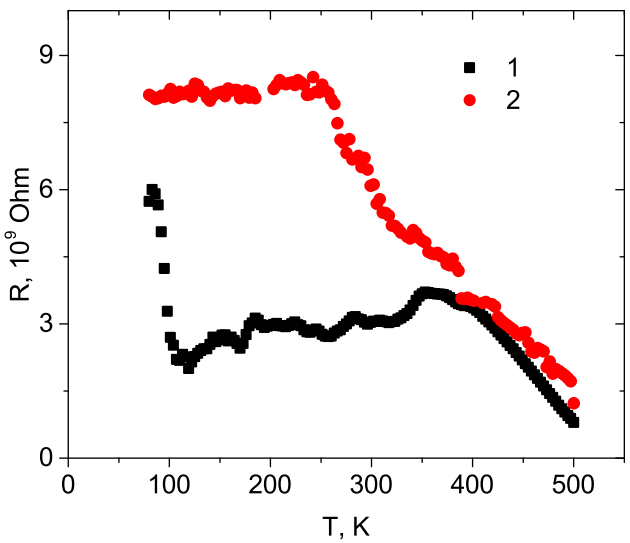

Fig. 13 Electrical resistance of the films on glass (1) and on garnet (2) versus temperature

films at 120 K. In the temperature range of 150–250 K, the bias field weakly depends on the magnetic field, which is stronger than the field of magnetization saturation in the films by an order of magnitude and is not related to magnetic domain walls. This field is induced by bivalent ions Fe^{2+} in octahedral sites. The *I–V* hysteresis is observed at different external electric field strengths (Figs. 14 and 16) and caused by the ferroelectric polarization. The resulting current consists of the charge transport current I_{ch} and the polarization current I_p: $I=I_{ch}+I_p$. The transport current obeys the Ohm's law ($I_{ch}=U/R$) and the polarization current is $I_p=dP/dt$. Thus, we have $I=U/R+I_p$ and the polarization current $I_p=I-U/R$ passes through the maximum in the voltage range ($-U_{min}$, U_{max}) (see Fig. 14c and insets in Fig. 16a, b). The maximum I_p value is attained near $U=0$. We establish the voltage dependence of the electric polarization from the relation $j=dP/dt=(dP/dU)\ (dU/dt)$, where $P=\int jdU/(\frac{dU}{dt})$, accurate to the constant factor.

The *I–V* characteristics were measured for 100 s with the linear time dependence of the voltage $U=-U_{min}+at$ and a linear increase in the current $I_{ch}=-I_m+at$, where I_m is the maximum current in absolute value, t is the time, upon the voltage variation from $-U_{min}$ to U_{max}. The polarization current changes according to the harmonic law $I_p=I_{pm}\cdot\cos(\omega t+\varphi)$, where $\omega=1/T$, T is the time for measuring the *I–V* characteristics, and φ is the phase (Figs. 14c and 16a). The hysteresis of the electric polarization and the phase shift between the external field and the polarization current are not observed in the single-crystal film grown on GGG up to T=280 K. The electric polarization $P(U)$ saturates above 150 V (Fig. 14d). In the polycrystalline film on glass, we observe the $P(U)$ hysteresis and phase shift between the polarization current and external field in this temperature range (Fig. 16d). In particular, with an increase in the external electric field, we have $\varphi=0.4\pi$, while with a decrease in the field, $\varphi=-\pi/2$ (insert in Fig. 16b). In the polycrystalline film, the displacement of domain walls in the electric field direction has a phase delay caused by their pinning on the grain boundaries. Thus, the effective coercive field in the polycrystalline film is stronger than in the film on GGG by 40% (Fig. 15). The maximum polarization currents differ by a factor of 1.5.

Upon heating above 280 K, the polarization current increases and a phase shift occurs in the single-crystal

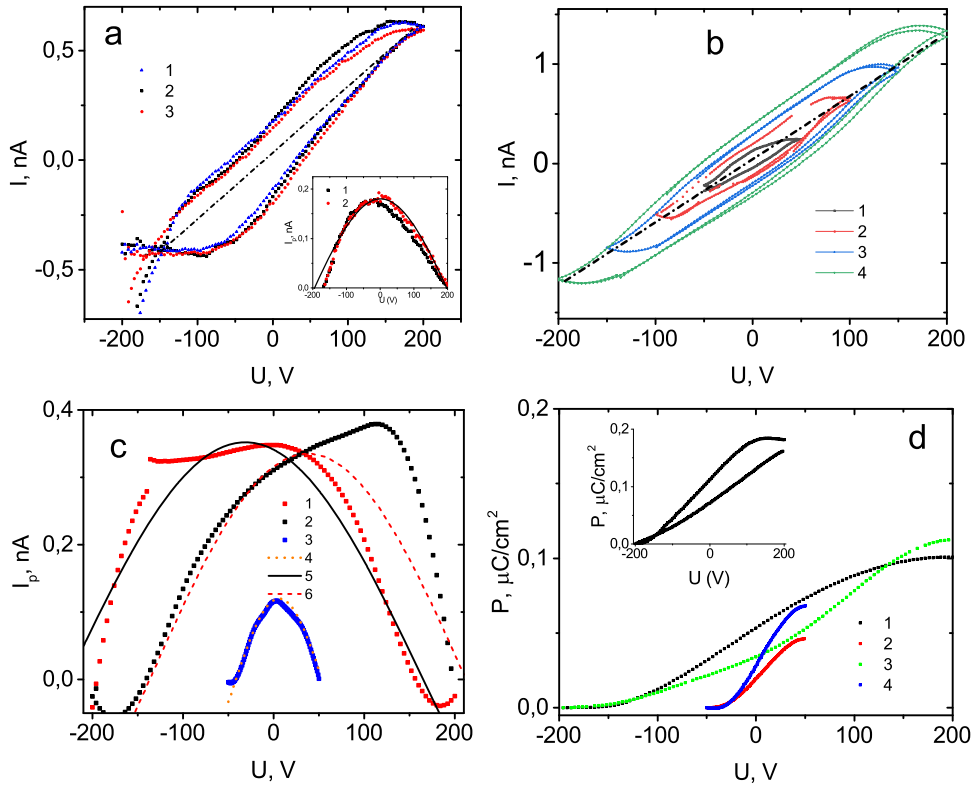

Fig. 14 *I–V* characteristic of the film on garnet at T=120 K, without field H=0 (1), H=12 kOe along the film (2), H=12 kOe perpendicular to the film (3) (**a**), at T=380 K at different voltages (**b**). The polarization current at T=380 K with increasing voltage from−200 to 200 V (1), with decreasing voltage from 200 to−200 V (2), I_p in the voltage range U_m=50 V, ($-U_m$ U_m) V (3); fitting function $I_p=I_{p0}$ cos ($\omega t+\phi$) with ϕ=0 (4), $\phi=\pi/8$ (5), $\phi=\pi/3$ (6) (**c**). The polarization of the film on a garnet versus electric voltage at T=120 K (1), T=300 K, U_m=50 V (2), U_m=200 V (3), T=380 K, U_m=50 V (4) (**d**) Insert (d): hysteresis of electric polarization at T=380 K. On insert (a): polarization current in absolute value at T=120 K with increasing voltage from−200 to 200 V (1), with decreasing voltage from 200 to−200 V (2); Fitting function $I_p=I_{p0}$ cos (ωt) (solid line). Current according to Ohm's law (dash dot)

film when measuring the *I–V* characteristics at high voltages in the range of (− 200, 200) V, which is absent in weak (− 50, 50 V) fields (Fig. 14c). The polarization current $I_p(U)$ in the single-crystal and polycrystalline films is described by a harmonic spectrum with lower frequencies and a phase shift of $\varphi=\pi/2$. The hysteresis of the *I–V* characteristic of the film on GGG decreases at T=460 K by an order of magnitude. In the polycrystalline film on glass, the nonlinearity of the $P(U)$ dependence vanishes at T>400 K.

5 Model

The ferroelectric properties are governed by the Bi–O bond via displacing oxygen ions and changing the electron density on sp orbitals of bismuth ions (alone pair). The magnetic properties are mainly determined by the exchange coupling of iron ions in the octahedral and tetrahedral sites through an oxygen anion (Fe–O–Fe). The bismuth ion is located in a dodecahedron and surrounded by eight oxygen ions. The compression, shear, or bending strain induced by the magnetoelastic interaction or electric field-induced piezoelectric effect will lead to the formation of an electric dipole on the Bi–O bond. In the vicinity of the cavity and at the film–substrate interface, the inversion center is absent on a length of 5–10 nm and the piezoelectric effect $P=\alpha E$ can occur; in the rest part of the film, the piezoelectric effect is induced by electrostriction. The strain is an even function of the polarization: $x=QP^2=Q(\varepsilon\varepsilon_0)^2E^2$.

In piezoelectrics, we have $P=dx$, where the piezoelectric modulus coefficient is $d\sim10^{-12}$ C/N. The relative change in the film linear sizes proportionally to the electric field is $X=KE$, where K is the

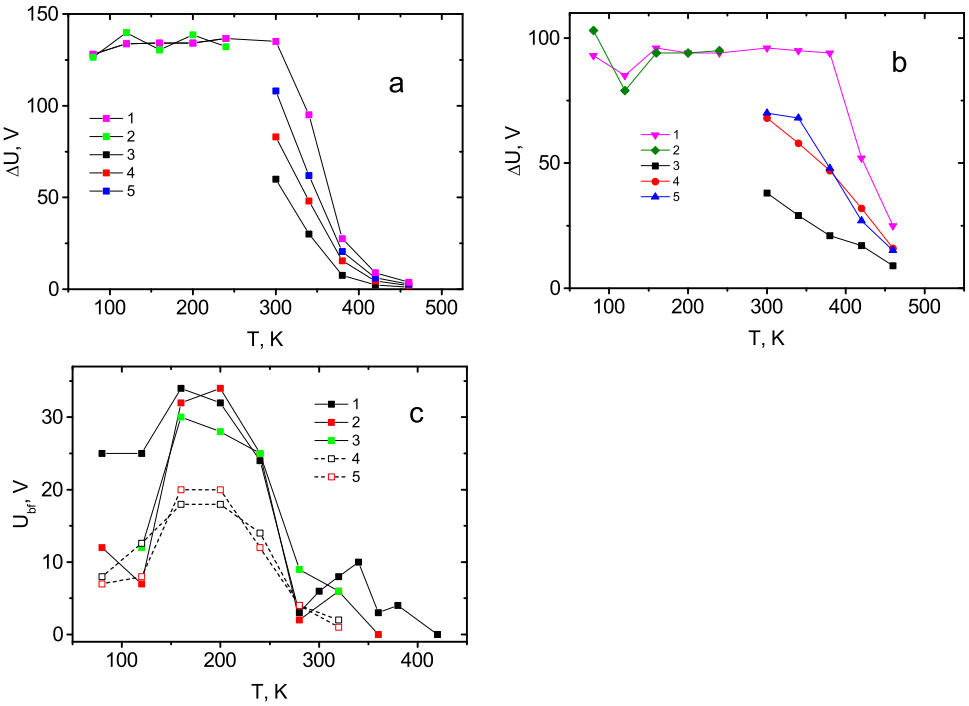

Fig. 15 Width of the *I–V* characteristic hysteresis at zero current in the film on glass (**a**) and on garnet (**b**) versus temperature without field H=0 (1), in a field directed perpendicular to the film H=12 kOe (2) with Um= 200 V, at voltage change from $-Um$ to Um, with H=0, Um= 50 V (3), 100 V (4), 150 V (5). Bias field (**c**) for a film on a garnet without a field H=0 (1), in a magnetic field perpendicular to the film H= 12 kOe (2), along the film H= 12 kOe (3); for a film on glass without a field H=0 (4), in a magnetic field perpendicular to the film H=12 kOe (5)

electromechanical coupling coefficient $K \sim 0.01$. In piezoelectrics, we have $\alpha = d/K \sim 10^{-10}$, which is larger than a value of α=(1–3) 10^{-12} for our samples by two orders of magnitude. This is related to the flexoelectric effect $P_{fl} = Ad\varepsilon_{\beta\gamma}/dx_{\sigma}$ [17], where $d\varepsilon_{\beta\gamma}/dx_{\sigma}$ is the strain gradient.

Ferroelectric domains are formed in the vicinity of the interface with polarization directed along the diagonals of the cube [111] (Fig. 17). Under the action of an external electric field, the domain width changes. The volume of the domain, the electric polarization of which is directed along the field, increases, and decreases with the opposite direction. Domain boundaries are pinned at charged defects, at Fe^{2+} ions. In YIG, divalent ions are in tetra- and octahedral positions [32]. The degenerate state of Fe^{2+} in the octahedron is lifted due to the spin–orbit interaction, and when the spins are ordered along the [111] axis, local trigonal distortion of the lattice occurs. The uniaxial anisotropy constant due to the spin–orbit interaction (λ), $D = \varepsilon_{\alpha\beta}\ \lambda^2/\Delta$, depends on the strain tensor $\varepsilon_{\alpha\beta}$, Δ is the energy between the ground and excited states. Electric polarization is proportional to the displacement of ions $P \sim U \sim \lambda^2 <S^z>^2/(\Delta k)$, k is the modulus of elasticity. This polarization induces the electric field that lead to shift the hysteresis loop in *I–V* characteristic.

Lowering the crystal symmetry to triclinic at 130 K in YIG [41] will cause a decrease in the t2g splitting of electronic states as a result of the spin–orbit interaction, which will lead to a decrease in the polarization and the electric field of bias.

Ionization of the $Fe^{2+} \rightarrow Fe^{3+}$ impurity state in the octahedron in the temperature range 270–300 K leads to anomalies in the impedance and capacitance of the films and to the disappearance of the asymmetry of the hysteresis loop. The change in the polarity of the external electric field (E_0) in the voltage range ΔU does not change the sign of the electric current, because the polarization current $I_p = dP/dt$ exceeds the charge transport current. Further heating of the film on glass leads to the removal of elastic stresses in the region of the film–substrate interface and to the disappearance of electric polarization in the range of 375–400 K temperatures. As a results, *I–V* hysteresis in a polycrystalline film is disappeared. This explains the fact of a sharp decrease in dielectric losses in the high-frequency region and electrical resistance above 400 K. Since the frequency of oscillations of magnetic domain walls in the yttrium iron garnet is $\omega_d \sim 10^6$ Hz, the value for lower-quality crystals is $\omega_d \sim 10^7$ Hz [42]. In the films, the polarization oscillation spectrum acquires a relaxation character. The dielectric loss decreases with a sharp decrease in the hysteresis width. The adhesion of the film on the

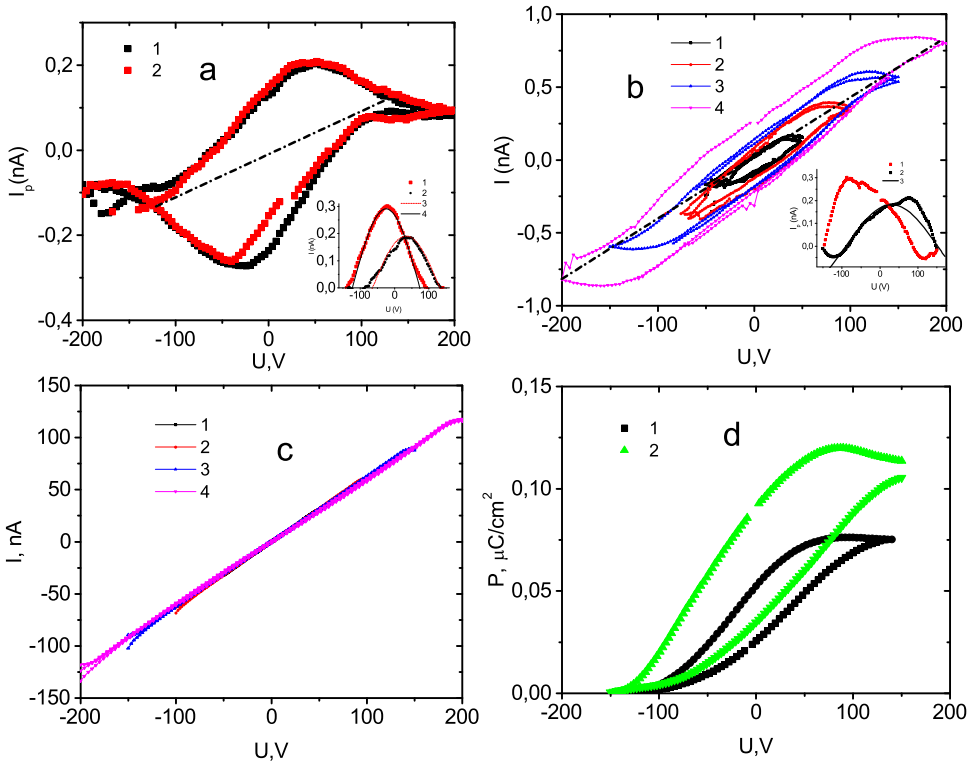

Fig. 16 *I–V* characteristic of the film on glass at T=120 K, without field H=0 (1), H=12 kOe perpendicular to the film (2) (**a**), at T=340 K (**b**) at T=460 K (**c**) at various voltages U_m=50 V (1), U_m=100 V (2), U_m=150 V (3), U_m=200 V (4). The polarization of the film on a garnet versus electric voltage at T=120 K (1), T=340 K (2) (**d**). Inset (a): polarization current in absolute value at T=120 K with increasing voltage from−200 to 200 V (1), with decreasing voltage from 200 to−200 V (2); Fitting function $Ip=I_{p0}\cos(\omega t+\phi)$ with $\phi=-0.54\pi$ (3), $\phi=0.4\pi$ (4). Inset (b): polarization current in absolute value at T=340 K with increasing voltage from−200 to 200 V (1), with decreasing voltage from 200 to−200 V (2); Fitting function $Ip=I_{p0}\cos(\omega t+\phi)$ with $\phi=-0.4\pi$ (3). Current according to Ohm's law (dash dot)

GGG substrate is much higher than the adhesion on glass; therefore, in a single-crystal film, polarization disappears at a higher temperature.

6 Conclusions

Two relaxation channels were found and attributed to the ferrite garnet lattice vibration modes and to the vibrations of ferroelectric domains observed by the tangent dielectric loss. A decrease in the impedance components in the film depending on the magnetic field is explained by the ME interaction induced of ferroelectric polarization. Ferroelectric domains are formed by elastic stresses as a result of the piezoelectric effect and the piezoelectric modules induced by electrostriction. Above room temperature, the migration polarization with a relaxation time spectrum was found from the impedance hodograph and the frequency dependence of the permittivity. In the megahertz frequency range, the dielectric loss is caused by ferroelectric domains. Two current channels, including the charge transport current and the polarization current, were found. The nonlinear electric field dependence of the polarization and the hysteresis were determined. The hysteresis of the *I–V* characteristic and the bias field are found. The hysteresis of the *I–V* is due to the polarization current that exceeds the charge transport current.

The *I–V* hysteresis and domains with the electric polarization in the polycrystalline film vanish at the lower temperature than in the single-crystal film. In the future, such films can be used in memristor devices, in commutators for switching current due to electric polarization.

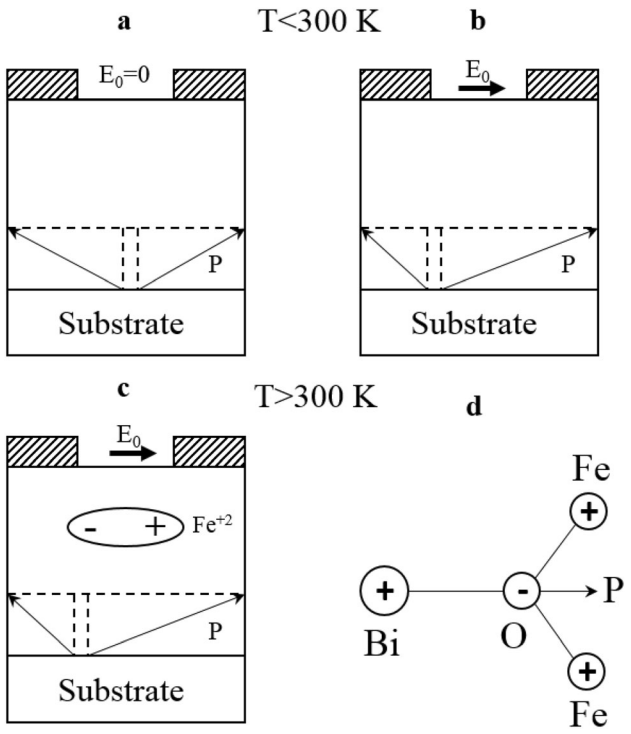

Fig. 17 Scheme of domains with a gradient of electric polarization at $T<T^*_1=300$ K, without the field $E=0$ (**a**), in an electric field (**b**), with a gradient of migration and dipole polarization $E=0$ (**c**). Dipole scheme on the Bi–O bond (**d**)

Acknowledgements

The electron microscopy investigations were carried out on the equipment of the Krasnoyarsk Territorial Center for Collective Use, Krasnoyarsk Scientific Center, Siberian Branch, Russian Academy of Sciences.

Author contributions

SSA supervised the experimental work. ANM, MNV performed all experimental work. TI grew films. The manuscript was written and discussed by all authors.

References

1. A. Fert, I.A. Campbell, Phys. Rev. Lett. **21**, 1190 (1968)
2. A. Avsar, H. Ochoa, F. Guinea, B. Özyilmaz, B.J. Van Wees, I.J. Vera-Marun, Rev. Mod. Phys. **92**, 021003 (2020)
3. D.B. Strukov, G.S. Snider, D.R. Stewart, R.S. Williams, Nature **453**, 80 (2008)
4. C. Torrezan, J.P. Strachan, G. Medeiros-Ribeiro, R.S. Williams, Nanotechnology **22**, 485203 (2011)
5. J.J. Yang, D.B. Strukov, D.R. Stewart, Nat. Nanotechnol. **8**, 13 (2013)
6. Y. Li, Z. Wang, R. Midya, Q. Xia, J.J. Yang, J. Phys. D **51**, 503002 (2018)
7. D.P. Kulikova, T.T. Gareev, E.P. Nikolaeva, T.B. Kosykh, A. V. Nikolaev, Z.A. Pyatakova, A.K. Zvezdin, A.P. Pyatakov, Phys. Status Solidi Rapid Res. Lett. **12**, 1800066 (2018)
8. N. Adachi, T. Okuda, V.P. Denysenkov, A. Jalali-Roudsar, A. M. Grishin, J. Magn. Magn. Mater. **242–245**, 775 (2002)
9. S. Logginov, G.A. Meshkov, A.V. Nikolaev, A.P. Pyatakov, JETP Lett. **86**, 115 (2007)
10. P. Pyatakov, D.A. Sechin, A.S. Sergeev, A.V. Nikolaev, E.P. Nikolaeva, A.S. Logginov, A.K. Zvezdin, EPL Europhys. Lett. **93**, 17001 (2011)
11. S. Sergeev, J. Phys. Conf. Ser. **929**, 012085 (2017)
12. F. Kabychenkov, F.V. Lisovskii, E.G. Mansvetova, JETP Lett. **97**, 265 (2013)
13. G.V. Arzamastseva, A.M. Balbashov, F.V. Lisovskii, E.G. Mansvetova, A.G. Temiryazev, M.P. Temiryazeva, J. Exp. Theor. Phys. **120**, 687 (2015)
14. B. Krichevtsov, V.V. Pavlov, R.V. Pisarev, Sov. J. Exp. Theor. Phys. Lett. **49**, 466 (1989)
15. E. Popova, A. Shengelaya, D. Daraselia, D. Japaridze, S. Cherifi-Hertel, L. Bocher, A. Gloter, O. Stéphan, Y. Dumont, N. Keller, Appl. Phys. Lett. **110**, 142404 (2017)
16. S.S. Aplesnin, A.N. Masyugin, M.N. Sitnikov, T. Ishibashi, JETP Lett. **110**, 223 (2019)
17. K. Tagantsev, Sov. Phys. Uspekhi **30**, 588 (1987)
18. T. Oikawa, S. Suzuki, K. Nakao, J. Phys. Soc. Japan **74**, 401 (2005)
19. S. Wittekoek, T.J.A. Popma, J.M. Robertson, P.F. Bongers, Phys. Rev. B **12**, 2777 (1975)
20. Y. Hosoe, K. Takanashi, H. Yasuoka, R. Suzuki, Y. Sugita, S. Chikazumi, J. Phys. Soc. Japan **55**, 731 (1986)
21. S.S. Aplesnin, A.N. Masyugin, M.N. Sitnicov, U.I. Rybina, T. Ishibashi, J. Magn. Magn. Mater. **464**, 44 (2018)
22. T. Ishibashi, A. Mizusawa, M. Nagai, S. Shimizu, K. Sato, N. Togashi, T. Mogi, M. Houchido, H. Sano, K. Kuriyama, J. Appl. Phys. **97**, 013516 (2005)
23. H. Kockar, T. Meydan, Phys. B **321**, 124 (2002)
24. T. Okuda, T. Katayama, K. Satoh, H. Yamamoto, J. Appl. Phys. **69**, 4580 (1991)
25. J. Chu, Y. Zhao, M.Z. Khan, X. Tang, W. Wu, J. Shi, Y. Wu, H. Huhtinen, H. Suo, Z. Jin, Cryst. Growth Des. **19**, 6752 (2019)
26. M. Sasaki, G. Lou, Q. Liu, M. Ninomiya, T. Kato, S. Iwata, T. Ishibashi, Jpn. J. Appl. Phys. **55**, 055501 (2016)
27. T. Yoshida, K. Oishi, T. Nishi, T. Ishibashi, EPJ Web of Conferences. EDP Sciences, vol. 75 (2014), p. 05009 (2014)
28. E.A. Manykin, V.B. Oshurko, Laser Phys. **17**, 842 (2007)

29. G.E. Walrafen, J. Chem. Phys. **47**, 114 (1967)
30. C. Steinbach, P. Andersson, J.K. Kazimirski, U. Buck, V. Buch, T.A. Beu, J. Phys. Chem. A **108**, 6165 (2004)
31. W.F. Kuhs, J.L. Finney, C. Vettier, D.V. Bliss, J. Chem. Phys. **81**, 3612 (1984)
32. Z.V. Gareyeva, R.A. Doroshenko, J. Magn. Magn. Mater. **268**, 1 (2004)
33. J.I. Pankove, *Optical Processes in Semiconductors* (New Jersey, Prentice-Hall, Englewood Cliffs, 1971), p. 422
34. V.V. Randoshkin, N.V. Vasil'eva, V.G. Plotnichenko, Y.N. Pyrkov, S.V. Lavrishchev, M.A. Ivanov, A.A. Kiryukhin, A. M. Saletskii, N.N. Sysoev, Phys. Solid State **46**, 1030 (2004)
35. R. Metselaar, P.K. Larsen, Solid State Commun. **15**, 291 (1974)
36. S. Suzuki, K. Nakao, J. Phys. Soc. Japan **69**, 532 (2000)
37. S.H. Wemple, S.L. Blank, J.A. Seman, W.A. Biolsi, Phys. Rev. B **9**, 2134 (1974)
38. R.F. Al'muhametov, K.P. Belov, N.V. Volkova, Solid State Phys. **25**, 1499–1502 (1983)
39. G.A. Babushkin, A.K. Zvezdin, R.Z. Levitin, JETP Lett. **80**, 1952 (1981)
40. N. Adachi, T. Ota, J. Ceram. Soc. Japan **122**, 40 (2014)
41. E. Kita, S. Takano, A. Tasaki, K. Siratori, K. Kohn, S. Kimura, J. Appl. Phys. **64**, 5661 (1988)
42. G. Gurevich, *Magnetic Resonance in Ferrites and Antiferromagnets* (Nauka, Moscow, 1973).

Publisher's Note Springer Nature remains neutral with regard to jurisdictional claims in published maps and institutional affiliations.